

Supplementary information

How do H₂ oxidation molecular catalysts assemble onto carbon nanotube electrodes? A crosstalk between electrochemical and multi-physical characterization techniques.

Ahmed Ghedjatti,^{1,2,3} Nathan Coutard,¹ Laura Calvillo,⁴ Gaetano Granozzi,⁴ Bertrand Reuillard,¹ Vincent Artero,¹ Laure Guetaz,⁵ Sandrine Lyonard,³ Hanako Okuno,² Pascale Chenevier^{3,*}

¹ Univ. Grenoble Alpes, CNRS, CEA, IRIG, Laboratoire de Chimie et Biologie des métaux, 38000 Grenoble, France

² Univ. Grenoble Alpes, CEA, IRIG, MEM, LEMMA, 38000 Grenoble, France

³ Univ. Grenoble Alpes, CEA, CNRS, IRIG, SYMMES, STEP, 38000 Grenoble, France

⁴ Department of Chemical Sciences, University of Padova, Via F. Marzolo 1, Padova 35131, Italy

⁵ Univ. Grenoble Alpes, CEA, LITEN, DTNM, 38000 Grenoble, France

* to whom correspondence should be addressed: pascale.chenevier@cea.fr

Table S1: XPS chemical analysis of MWNT-p, MWNT-a, MWNT-NiArg

atomic %	C	C sp ²	other C	N	O	Ni	P	F	B
MWNT-p	98.7	87.4	11.2		1.3				
MWNT-a	93.5	80.8	12.7	1.1	5.4				
MWNT-NiArg	75.8	46.9	29.0	6.5	9.2	0.8	3.3	3.2	1.2
NiArg elemental ratio from formula C ₅₆ H ₁₁₄ B ₂ F ₈ N ₁₆ NiO ₈ P ₄	44.8	0	44.8	12.8	6.4	0.8 ^a	3.2	6.4	1.6

^a The **NiArg** elemental composition from its raw formula was scaled to match the Ni content with the measured Ni content in MWNT-NiArg, for easier comparison.

Table S2: detailed XPS analysis of the C1s spectra.

atomic %	C sp ² 284.2eV	C sp ³ 285.6eV	C-OH/C-N 286.5eV	C=O 287.8eV	O-C=O 288.9eV
MWNT-p	88.6	4.1	4.5	2.2	0.6
MWNT-a	86.4	5.1	5.1	2.2	1.2
MWNT-NiArg	61.7	18.8	13.3	4.1	2.1

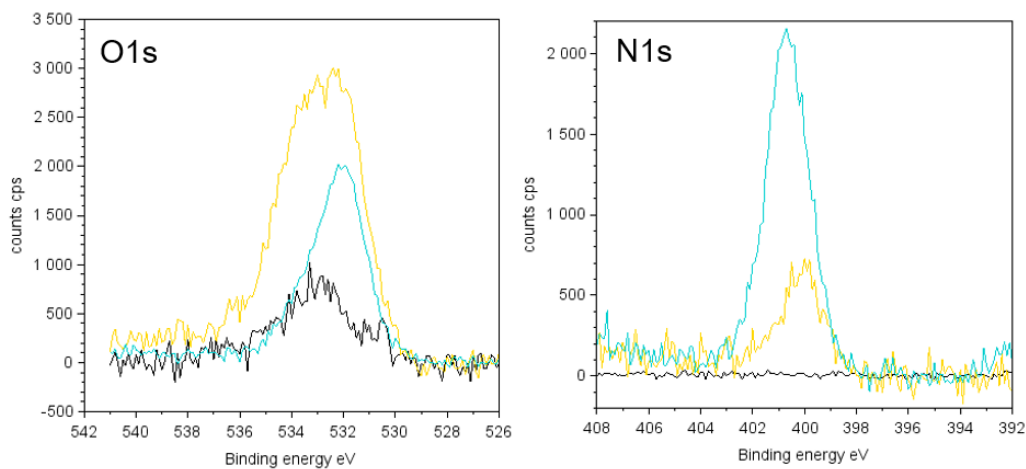


Figure S1: XPS spectra of MWNT-p (black line), MWNT-a (yellow line) and MWNT-NiArg (cyan line) of regions O1s and N1s.

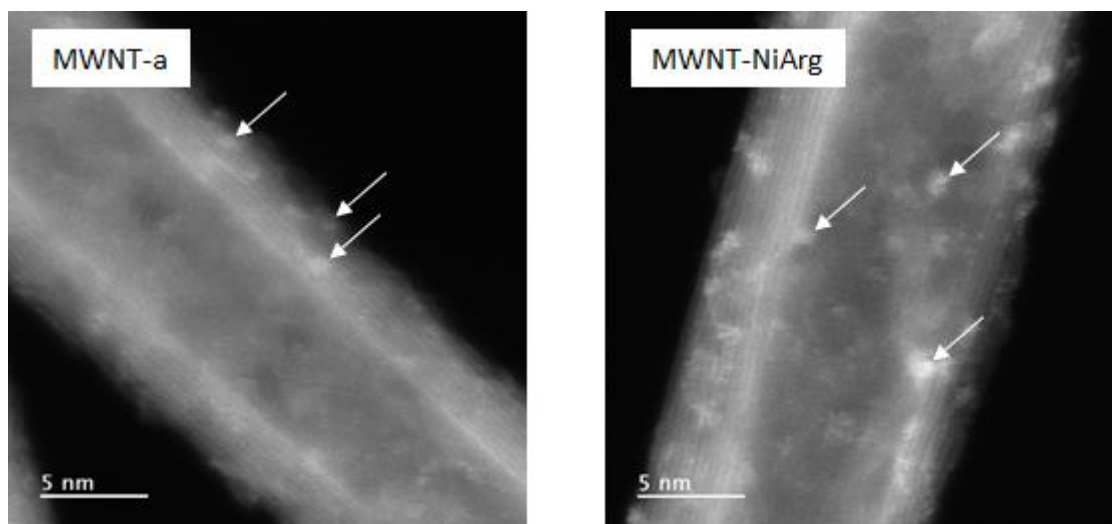


Figure S2: HAADF-STEM images of MWNT-a and MWNT-NiArg after electron irradiation. The agglomerated functionalized species are shown by arrows, whereas the contrast of aggregates in MWNT-NiArg is stronger than those in MWNT-a.

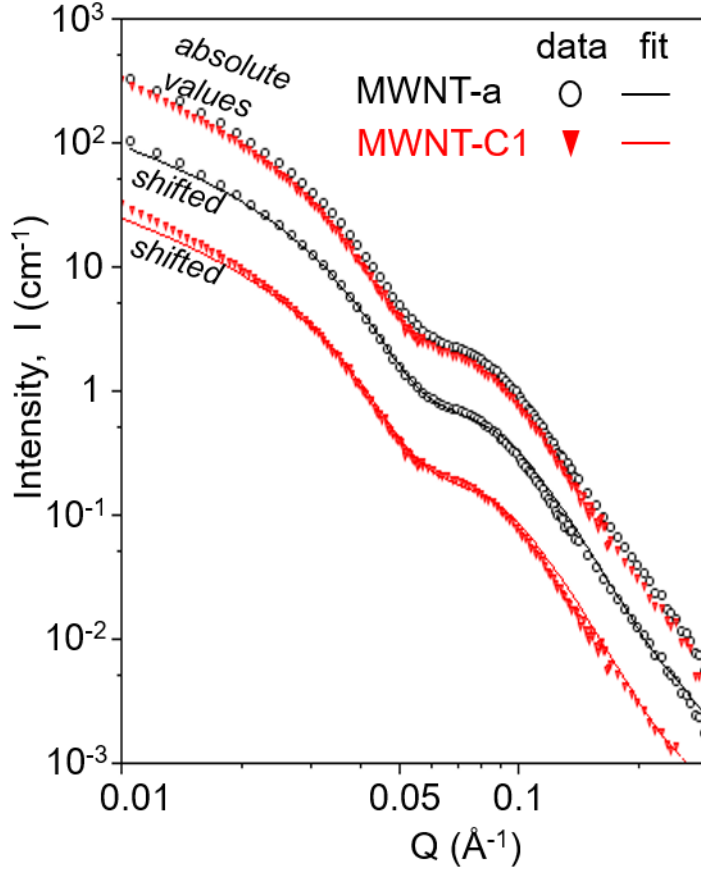


Figure S3: SANS profiles for MWNT-a (circles) and MWNT-C1 (triangles) in the fully hydrogenated solvent. The top curves are data in absolute intensity, showing how the data for both samples superimposed. The curves below are shifted copies with their corresponding fits. The fit to a core-shell cylinder profile¹ is excellent from 0.02 to 0.3 Å⁻¹. An additional signal appears at lower Q, due to MWNT aggregation.

SANS fitting parameters. SANS profiles were fitted using the SASView software, with the core-shell cylinder model. This corresponds to the following model:

$$I(q, \alpha) = \frac{1}{V_s} F^2(q, \alpha) \cdot \sin(\alpha) + \text{background}$$

where

$$F(q, \alpha) = (\rho_c - \rho_s) V_c \frac{\sin\left(\frac{1}{2} L q \cos \alpha\right) 2J_1(q R s \sin \alpha)}{\frac{1}{2} L q \cos \alpha \quad q R s \sin \alpha} + (\rho_s - \rho_{\text{soln}}) V_s \frac{\sin\left(q \left(\frac{1}{2} L + T\right) \cos \alpha\right) 2J_1(q(R + T) s \sin \alpha)}{q \left(\frac{1}{2} L + T\right) \cos \alpha \quad q(R + T) s \sin \alpha}$$

and

$$V_s = \pi(R + T)^2(L + 2T)$$

and α is the angle between cylinder axis and q , V_s is the total volume, V_c is the volume of the core, L is the length of the core, R is the radius of the core, T is the thickness of the shell, ρ_c is the scattering length density of the core, ρ_s is the scattering length density of shell, ρ_{soln} is the scattering length density of the solvent, and *background* is the background level. J_1 is the first order Bessel function.

Size dispersity was considered with a Boltzmann distribution for the core and shell diameters. A dispersion factor of PD=0.4 was found optimal. First, the SLD of the core and shell were adjusted by fitting the model on the MWNT-a series. The best fitting parameters are presented in Fig. S2. Only the core SLD depends significantly on the %D, showing that the core of the MWNT is partly open to solvent penetration.

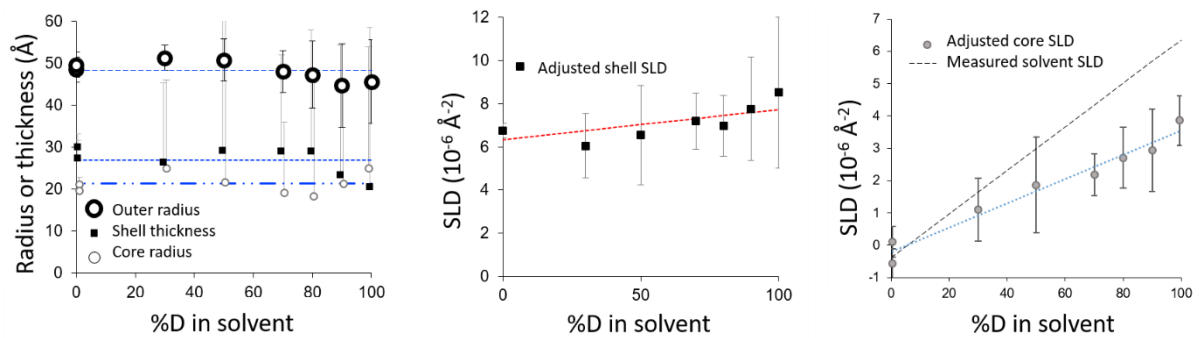


Figure S4: best fitting parameters for the SANS profiles of the MWNT-a series.

Using these shell SLD and average core radius and shell thickness values and distributions, the SANS profiles of the MWNT-NiArg series were fitted with adjustment of the core and solvent SLD. The best fit are presented on Fig. S3. It can be seen that the adjusted core SLD was the same for MWNT-NiArg and MWNT-a. The solvent SLD was found to follow the pure solvent, showing no effect of NiArg on the shell-solvent contrast.

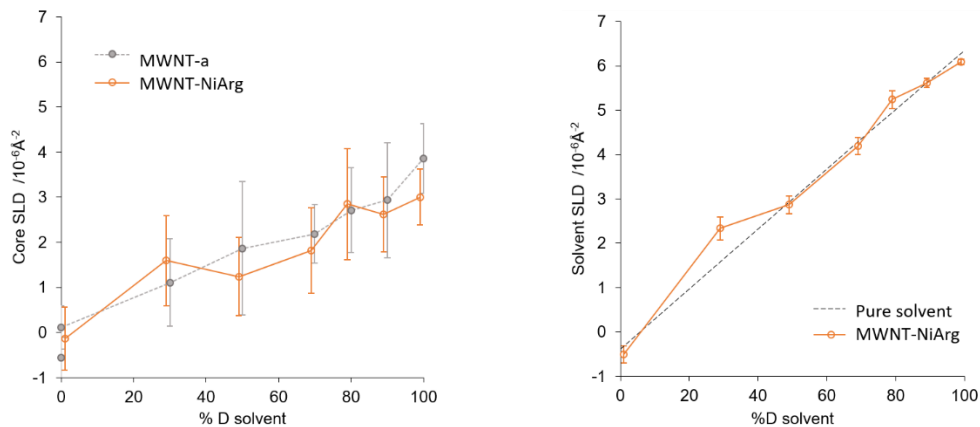


Figure S5: best fitting parameters for the SANS profiles of the MWNT-NiArg series.

MWNT-NiArg in the presence of Nafion.

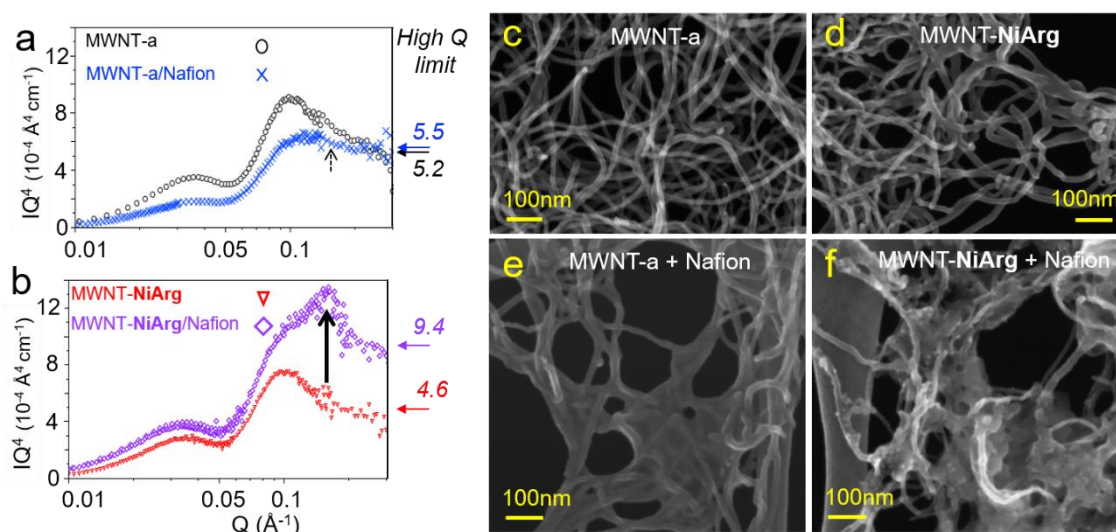


Figure S6: NiArg interfering in Nafion-MWNT interaction in the catalytic layer. (a,b) Porod plots of MWNT-a (a), and MWNT-NiArg (b) without and with Nafion in a non-deuterated solvent. The Nafion nanostructure peak (vertical arrow) appears on the MWNT-NiArg/Nafion profile (b), but it is missing on the MWNT-a/Nafion profile (a). Horizontal arrows on the right indicate the IQ^4 limit at high Q for each Porod profile. (c,d,e,f) SEM images of MWNT-a (c) and MWNT-NiArg (d), and MWNT-a (e) and MWNT-NiArg (f) with Nafion in a 1:1 MWNT/Nafion mass ratio.

The MWNT-NiArg composite was mixed with Nafion as in inks for the preparation of a fuel cell anode catalytic layer. We showed previously that the presence of MWNTs can strongly disturb the self-organization of Nafion.¹ Indeed, it was shown that Nafion has a strong affinity for the MWNT surface² and can displace or hinder some MWNT-grafted catalysts.³

Difference between MWNT-a/Nafion and MWNT-NiArg/Nafion by SANS: As an amphiphilic compound, Nafion adopts, in the presence of water, a nanostructure in which the hydrophobic backbone forms a network surrounding pockets of water. The high contrast in SLD between water and fluorinated backbone and the regular size of the aqueous pockets produces a strong SANS signal,^{1,4} with a characteristic peak at $Q = 0.16 \text{ \AA}^{-1}$ when Nafion is in an excess of water. The Porod plot (IQ^4 vs Q) of the MWNT-NiArg/Nafion sample show this Nafion peak as expected (arrow in Fig. S6b), while the peak is remarkably absent from the profile of MWNT-a/Nafion (Fig. S6a). This can be explained by the strong hydrophobic interaction between the MWNT surface and the fluorinated Nafion backbone, as previously reported.¹⁻³ Under our conditions (a 1:1 mass ratio with MWNT), all of the ionomer is adsorbed at the carbon nanotube surface and no self-organized Nafion structure can be formed. On the contrary, the presence of the cationic NiArg layer at the surface of MWNT-NiArg prevents such hydrophobic interaction, so that Nafion can self-organize in its usual nanostructure.

The Porod plots of the SANS data brings a quantitative information on the sample's surface area. The Porod profile plateaus at a high Q value, into a signal summing all the contrasted interfaces in the sample. The Porod intensity at the plateau is thus proportional to the specific area of the material and to its SLD contrast. Here, the plateau is measured around $Q = 0.2-0.3 \text{ \AA}^{-1}$, after the characteristic core-shell cylinder double peak, as noise becomes predominant at $Q > 0.3 \text{ \AA}^{-1}$ (values aside Fig. S6a-b). As the SLD contrasts measured in this sample series by fitting the core-shell cylinder profile were very close (6 to $8 \cdot 10^{-6} \text{ \AA}^{-2}$), the IQ^4 plateau at high Q is a good indication of the specific area of the

material. It can be noticed that this limit is very close for the MWNT-a, MWNT-NiArg and MWNT-a/Nafion. This stable specific area indicates that modifications of the composite mainly happen in the form of layer deposition onto the MWNTs. By contrast, the specific area of the MWNT-NiArg/Nafion is almost doubled, showing the creation of a large amount of nanostructures independent of the MWNTs.

Difference between MWNT-a/Nafion and MWNT-NiArg/Nafion by SEM: The MWNT-a/Nafion sample shows a similar aspect as MWNT-a (Fig. 6c) with an additional thin and homogeneous coating (Fig. S6e). Conversely, the MWNT-NiArg/Nafion sample contains additional globular structures surrounding the MWNTs (Fig. S6f), that does not appear on MWNT-NiArg (Fig. S6d).

Difference between MWNT-a/Nafion and MWNT-NiArg/Nafion in electrocatalysis: We quantified the amount of electrochemically wired NiArg in the MWNT-NiArg film by studying its reversible electrochemical signature at neutral pH and under argon (Fig. 2a). The integration of the oxidation wave of the reversible redox event at $E_{1/2} = 0.04\text{V}$ vs RHE, attributed to the $2e^-/2\text{H}^+$ Ni-centered redox process of NiArg,⁵ corresponds to a density of electrochemically active catalyst of 42 and 32 nmol_{NiArg}/mg_{MWNT} without and with Nafion, respectively. The share of electrochemically connected catalyst thus represents about 20% of the total amount of deposited catalyst in MWNT-NiArg, and 15% for MWNT-NiArg/Nafion. These are reasonable yields as compared to other molecular systems.^{1,6,7}

References

- (1) Coutard, N.; Reuillard, B.; Huan, T. N.; Valentino, F.; Jane, R. T.; Gentil, S.; Andreiadis, E. S.; Le Goff, A.; Asset, T.; Maillard, F.; Jusselme, B.; Morozan, A.; Lyonnard, S.; Artero, V.; Chenevier, P. Impact of Ionomer Structuration on the Performance of Bio-Inspired Noble-Metal-Free Fuel Cell Anodes. *Chem Catalysis* **2021**, *1*, 1. <https://doi.org/10.1016/j.checat.2021.01.001>.
- (2) Wang, J.; Musameh, M.; Lin, Y. Solubilization of Carbon Nanotubes by Nafion toward the Preparation of Amperometric Biosensors. *Journal of the American Chemical Society* **2003**, *125* (9), 2408–2409. <https://doi.org/10.1021/ja028951v>.
- (3) Osmieri, L.; Wang, G.; Cetinbas, F. C.; Khandavalli, S.; Park, J.; Medina, S.; Mauger, S. A.; Ulsh, M.; Pylypenko, S.; Myers, D. J.; Neyerlin, K. C. Utilizing Ink Composition to Tune Bulk-Electrode Gas Transport, Performance, and Operational Robustness for a Fe–N–C Catalyst in Polymer Electrolyte Fuel Cell. *Nano Energy* **2020**, *75*, 104943. <https://doi.org/10.1016/j.nanoen.2020.104943>.
- (4) Rubatat, L.; Gebel, G.; Diat, O. Fibrillar Structure of Nafion: Matching Fourier and Real Space Studies of Corresponding Films and Solutions. *Macromolecules* **2004**, *37* (20), 7772–7783. <https://doi.org/10.1021/ma049683j>.
- (5) Gentil, S.; Lalaoui, N.; Dutta, A.; Nedellec, Y.; Cosnier, S.; Shaw, W. J.; Artero, V.; Le Goff, A. Carbon-Nanotube-Supported Bio-Inspired Nickel Catalyst and Its Integration in Hybrid Hydrogen/Air Fuel Cells. *Angew Chem Int Ed Engl* **2017**, *56* (7), 1845–1849. <https://doi.org/10.1002/anie.201611532>.
- (6) Chenevier, P.; Mughlerli, L.; Darbe, S.; Darchy, L.; Dimanno, S.; Tran, P. D.; Valentino, F.; Iannello, M.; Volbeda, A.; Cavazza, C.; Artero, V. Hydrogenase Enzymes: Application in Biofuel Cells and Inspiration for the Design of Noble-Metal Free Catalysts for H₂ Oxidation. *Comptes Rendus Chimie* **2013**, *16* (5), 491–505.
- (7) Poulpiquet, A.; Marques-Knopf, H.; Wernert, V.; Giudici-Ortoni, M. T.; Gadiou, R.; Lojou, E. Carbon Nanofiber Mesoporous Films: Efficient Platforms for Bio-Hydrogen Oxidation in Biofuel Cells. *Physical chemistry chemical physics : PCCP* **2013**, *16* (4), 1366–1378. <https://doi.org/10.1039/c3cp54631d>.

